Research Article

Ruimeng Wang, Li Pan, Wenhui Niu, Rumeng Li, Xiaoyang Zhao, Xiqing Bian, Chong Yu, Haoming Xia, and Taizheng Chen*

Monitoring the spatiotemporal dynamics of surface water body of the Xiaolangdi Reservoir using Landsat-5/7/8 imagery and Google Earth Engine

https://doi.org/10.1515/geo-2020-0305
received June 07, 2021; accepted October 02, 2021

Abstract: Xiaolangdi Reservoir is a key control project to control the water and sediment in the lower Yellow River, and a timely and accurate grasp of the reservoir's water storage status is essential for the function of the reservoir. This study used all available Landsat images (789 scenes) and adopted the modified normalized difference water index, enhanced vegetation index, and normalized difference vegetation index to map the surface water from 1999 to 2019 in Google Earth Engine (GEE) cloud platform. The spatiotemporal characteristics of the surface water body area changes in the Xiaolangdi Reservoir in the past 21 years are analyzed from the water body type division, area change, type conversion, and the driving force of the Xiaolangdi water body area changes was analyzed. The results showed that (1) the overall accuracy of the water body extraction method was 98.86%, and the kappa coefficient was 0.96; (2) the maximum water body area of the Xiaolangdi Reservoir varies greatly between inter-annual and intra-annual, and seasonal water body and permanent water body have uneven spatiotemporal distribution; (3) in the conversion of water body types, the increased seasonal water body area of the Xiaolangdi Reservoir from 1999 to 2019 was mainly formed by the conversion of permanent water body, and the reduced permanent water body area was mainly caused by non-water conversion; and (4) the change of the water body area of the Xiaolangdi Reservoir has a weak negative correlation with natural factors such as precipitation and temperature, and population. It is positively correlated with seven indicators such as runoff and regional gross domestic product (GDP). The findings of the research will provide necessary data support for the management and planning of soil and water resources in the Xiaolangdi Reservoir.

Keywords: Landsat imagery, Google Earth Engine, water body extraction, spatiotemporal change, Xiaolangdi Reservoir

1 Introduction

Surface water refers to rivers, lakes, ponds, reservoirs, swamps, glaciers, and other water bodies that exist on the Earth's surface. They are tremendously important water resources for agriculture, aquaculture, industrial production, and terrestrial ecosystems. Xiaolangdi Reservoir is located in the key position of controlling water and sediment in the lower reaches of the Yellow River, and it is the only control project under Sanmenxia that can obtain large storage capacity [1–3]. Xiaolangdi Reservoir is a comprehensive water control project for flood control, ice jam prevention, sediment reduction, runoff regulation, water supply, and power generation in the lower reaches of the reservoir [1,2,4]. It has superior natural conditions and an important strategic position. Timely and accurate acquisition of the reservoir water storage situation is essential to

* **Corresponding author: Taizheng Chen,** College of Geography and Environmental Science, Henan University, Kaifeng 475004, China, e-mail: 10130043@vip.henu.edu.cn, tel: +86-371-2388-1850
Ruimeng Wang, Li Pan, Wenhui Niu, Rumeng Li, Xiaoyang Zhao, Xiqing Bian, Chong Yu: College of Geography and Environmental Science, Henan University, Kaifeng 475004, China
Haoming Xia: College of Geography and Environmental Science, Henan University, Kaifeng 475004, China; Henan Key Laboratory of Earth System Observation and Modeling, Henan University, Kaifeng 475004, China; Key Laboratory of Geospatial Technology for the Middle and Lower Yellow River Regions (Henan University), Ministry of Education, Kaifeng 475004, China; Key Research Institute of Yellow River Civilization and Sustainable Development and Collaborative Innovation Center on Yellow River Civilization Jointly Built by Henan Province and Ministry of Education, Henan University, Kaifeng 475004, China

the function of the reservoir [1,3,5,6]. The changes in the scope and area of the Xiaolangdi Reservoir can reflect the comprehensive role of climate and human activities in the water cycle and ecosystem [7].

Remote sensing image data have the characteristics of comprehensive coverage, high revisit frequency, rich information, and low cost, which supplies the possibility for quantitative estimation of long time series of reservoir water body areas [4,8–10]. At present, the multisource remote sensing data, Systeme Probatoire d'Observation de la Terre [11], Landsat [12–17], Moderate Resolution Imaging Spectroradiometer (MODIS) [18–21], Sentinel [22–25], are applied for extracting water body area and change monitoring [26–32]. The Google Earth Engine (GEE) cloud computing platform is developed by Google. Based on JavaScript or Python algorithm development tools on the web, it can realize online visualization calculation and analytical processing of remote sensing data [14,33–38]. GEE has high-performance parallel computing functions, massive remote sensing data, geospatial data, and free use, and it provides a new way for long-term sequence and large-scale remote sensing analysis. It has multi-source remote sensing data sets such as Landsat, MODIS, Sentinel, and other remote sensing data sets [15,16,36,39–42]. Up to now, GEE was widely used in large-scale geoscientific studies including urban land cover, crop monitoring, wetland monitoring, forest cover mapping, and water body monitoring [43,44].

Water body extraction methods include water body extraction algorithms based on band combination (single-band threshold method, multiband spectral relation method, water index method, and threshold method) and machine learning algorithm (support vector machines, random forest, deep learning) [44–47]. The water body index can quickly obtain the distribution range of the water body through simple band calculation and threshold processing. For example, Mefeeters et al. [48] proposed the normalized difference vegetation index (NDVI) index, which suppresses vegetation and highlights water information but the suppression effect in buildings was not good. Xu [49] proposed that the modified normalized difference water index (MNDWI) can reduce the interference of soil and buildings, but it is not effective in distinguishing water bodies from vegetation. This study uses a combination of MNDWI, normalized difference vegetation index (NDVI) [50], and enhanced vegetation index (EVI), which can eliminate land noise and decrease wetlands mixed with water bodies and vegetation to improve the accuracy of the water body index.

Based on the GEE platform in this study, 789 remote sensing images of Landsat Thematic Mapper (TM), Landsat Enhanced Thematic Mapper (ETM+), and Landsat Operational Land Imager (OLI) captured from 1999 to 2019 were obtained by JavaScript programming operation. The method of combining the MNDWI, NDVI, and EVI was used to extract the accuracy of surface water body extraction. The spatiotemporal distribution patterns of the surface water body in the Xiaolangdi Reservoir in recent 21 years were obtained, and three water body types were generated according to water body frequency: maximum water body, seasonal water body, and permanent water body. The inter-annual and intra-annual variation characteristics of the three types of water bodies and the transformation types of the Xiaolangdi Reservoir are analyzed, and the driving force of the change of Xiaolangdi water bodies is analyzed. It provides a scientific basis for ecological protection, water resource management, economic activities, and decision-making and planning in the Xiaolangdi area.

2 Materials and methods

2.1 Study area and data

2.1.1 Study area

Xiaolangdi Reservoir is the last Gorge Reservoir in the middle reaches of the Yellow River (Figure 1a); it is 40 km north of Luoyang City, 130 km from the Sanmenxia water control project, and 128 km from Huayuankou Station in Zhengzhou, Henan Province (Figure 1b–d) [1,4–7,32]. Xiaolangdi Reservoir is a large-scale comprehensive water conservancy project, which mainly focuses on flood control, ice jam prevention, and silt reduction, as well as water supply, irrigation, power generation, harm elimination, and benefit elimination [4,6]. The main project of the Xiaolangdi Reservoir started in September 1991, began to store water in October 1999, and completed the main project by the end of 2001. The total storage capacity of the Xiaolangdi Reservoir is $12.65 \times 10^8\ m^3$, the long-term effective storage capacity is $5.1 \times 10^8\ m^3$, and the control basin area is $69.4 \times 10^4\ km^2$, accounting for 92.3% of the Yellow River Basin Area [3,5]. Xiaolangdi Reservoir's average annual accumulated precipitation from 1999 to 2019 was 613 mm, and the annual average temperature was 14.14°C.

2.1.2 Data sources

This study used all available Landsat TM, ETM+, and OLI surface reflectance images of the entire Xiaolangdi

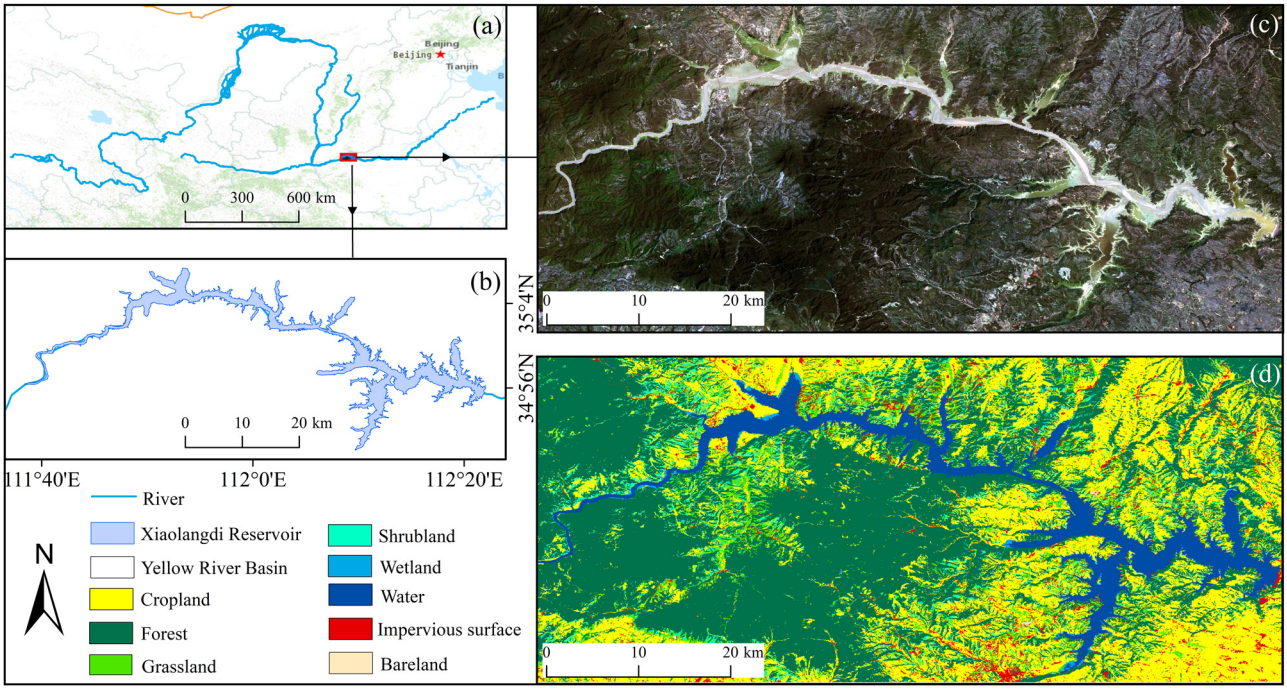

Figure 1: Map of (a) the Yellow River Basin; (b) location of the Xiaolangdi Reservoir; (c) false color image of the Xiaolangdi Reservoir; and (d) GlobeLand 30 of the Xiaolangdi Reservoir.

Reservoir in the GEE platform from 1999 to 2019. The Landsat TM and ETM+ surface reflectance datasets were generated from the Landsat ecosystem disturbance adaptive processing system algorithm, and the Landsat OLI surface reflectance products were generated from the Landsat surface reflectance code algorithm [51,52]. For each scene image, the function of the mask algorithm method is used to mask the cloud, cloud shadow, and snow pixels in the data. The high-quality image data after the mask has a good effect and is suitable for change detection of the land satellite data. The total number of these images was 789, including 224 Landsat TM from 1999 to 2013, 326 Landsat ETM+ from 1999 to 2019, and 239 Landsat OLI from 2013 to 2019. The spatial distribution (Figure 2a and b), temporal distribution (Figure 2c), and seasonal distribution (Figure 2d) of the Xiaolangdi Reservoir total observation count from 1999 to 2019.

Moreover, the Sentinel-2 images with a spatial resolution of 10 m were used to evaluate the accuracy of the extracted water bodies in the Xiaolangdi Reservoir. The 3 h Global Land Data Assimilation System (GLDAS) from 1999 to 2019 with a spatial resolution of 0.25° was used to analyze the temporal trend of precipitation and temperature in the Xiaolangdi Reservoir [53]. The 2010 Global 30 m land cover remote sensing data product (GlobeLand30) (http://www.globallandcover.com) was used to classify water bodies and non-water bodies [54,55].

2.2 Methods

2.2.1 Water body extraction algorithm

The study used an MNDWI (equation (1)), NDVI (equation (2)), and EVI (equation (3)). If a pixel meets the following criteria: EVI < 0.1 and (MNDWI > EVI or MNDWI > NDVI), then it was classified as a water body [14,16,36,56]:

$$\mathrm{MNDWI} = \frac{(\rho_{\mathrm{Green}} - \rho_{\mathrm{Swirl}})}{(\rho_{\mathrm{Green}} + \rho_{\mathrm{Swirl}})}, \tag{1}$$

$$\mathrm{NDVI} = \frac{(\rho_{\mathrm{Nir}} - \rho_{\mathrm{Red}})}{(\rho_{\mathrm{Nir}} + \rho_{\mathrm{Red}})}, \tag{2}$$

$$\mathrm{EVI} = 2.5 \times \frac{\rho_{\mathrm{Nir}} - \rho_{\mathrm{Red}}}{\rho_{\mathrm{Nir}} + 6 \times \rho_{\mathrm{Red}} - 7.5 \times \rho_{\mathrm{Blue}} + 1}, \tag{3}$$

where ρ_{Red}, ρ_{Green}, ρ_{Blue}, ρ_{Nir}, and ρ_{Swirl} are the reflectance of the red band (0.63–0.69 µm), green band (0.52–0.6 µm), blue band (0.45–0.52 µm), near-infrared band 1 (0.77–0.9 µm), and shortwave infrared band 1 (1.55–1.75 µm), respectively.

2.2.2 Change analysis of the surface water body

According to the long-term surface water bodies in the Xiaolangdi Reservoir, the water frequency (WF, equation (1)) ranges from 0 to 100%, According to WF, surface

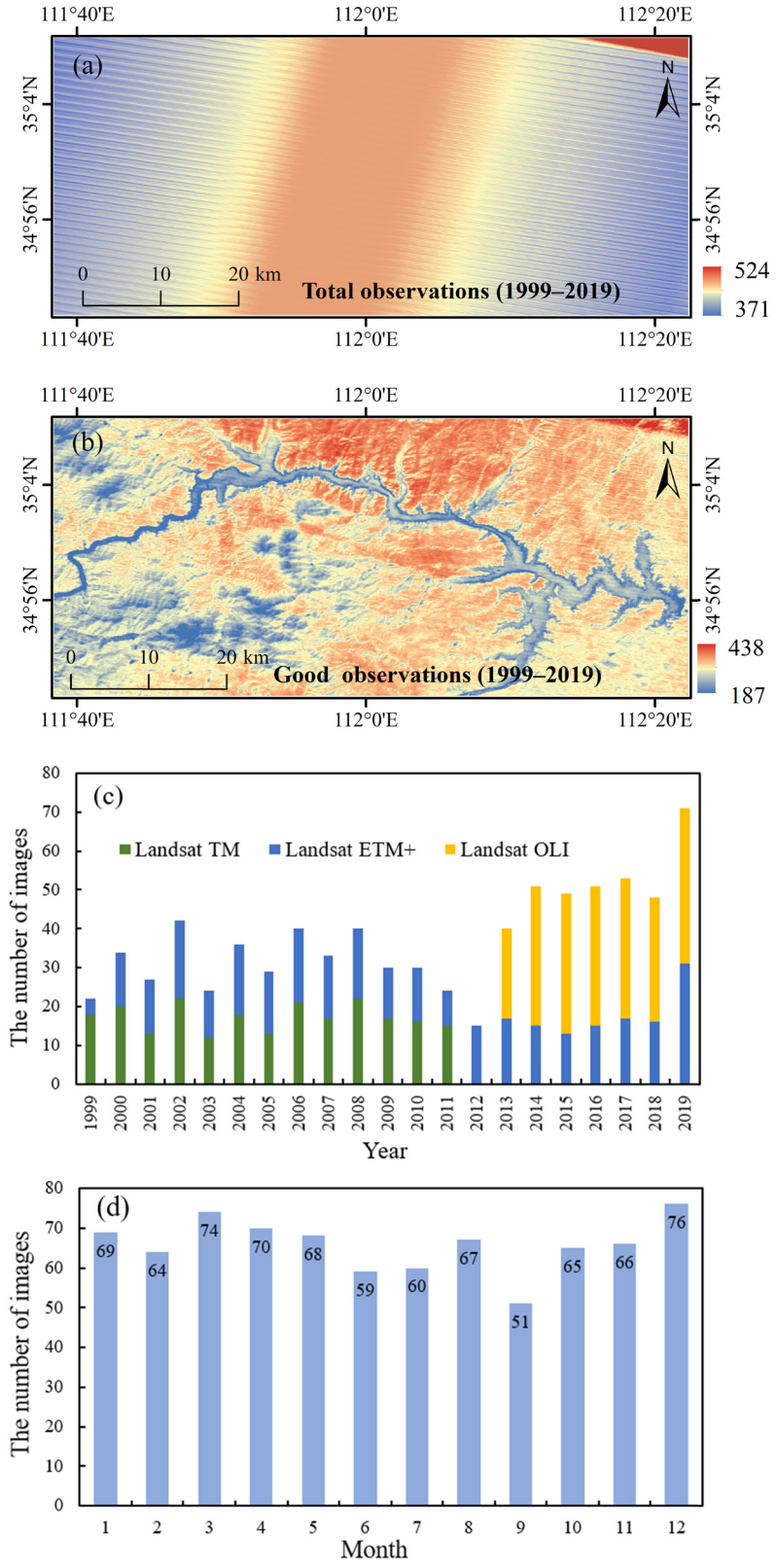

Figure 2: The Landsat images of the study area from 1999 to 2019: (a) spatial distribution of the number of all Landsat images; (b) spatial distribution of the number of high-quality Landsat images; (c) the temporal distribution of Landsat images; and (d) the seasonal distribution of Landsat images.

water body can be divided into three types: maximum water body (WF ≥ 25%), seasonal water body (25% < WF ≤ 75%), and permanent water body (WF ≥ 75%) [14,36,40].

$$\mathrm{WF} = \frac{\sum N_{\mathrm{Water}}}{\sum N_{\mathrm{Good}}} \times 100\%, \tag{4}$$

where $\sum N_{\mathrm{Water}}$ represents the number of times that all images were identified as water bodies during the year, and $\sum N_{\mathrm{Good}}$ represents the number of high-quality images during the year.

2.2.3 Dynamic degree of the surface water body

The changes in the surface water body mainly include type, area, dynamic degree, and time and space. The dynamic degree of a single surface water body expresses the change of a given surface water body type within a certain period. The surface water body change transfer matrix describes the surface water body area change [57].

(1) The dynamic degree of a single surface water body is expressed by the formula (equation (5))

$$K = \frac{S_b - S_a}{S_a} \times \frac{1}{T} \times 100\%, \tag{5}$$

where S_a and S_b are the areas of surface water body types at the beginning and end of the study, and T is the length of the study period.

(2) Surface water body transfer matrix.

The transfer matrix of the surface water body is the mutual conversion relationship between surface water body types in the same area in different periods. By establishing the transfer matrix of the surface water body in two periods, the area changes in different surface water body types in this period are analyzed (equation (6)):

$$S_{ij} = \begin{bmatrix} S_{11} & S_{12} & \cdots & S_{1n} \\ S_{21} & S_{22} & \cdots & S_{2n} \\ \cdots & \cdots & \cdots & \cdots \\ S_{n1} & S_{n2} & \cdots & S_{nn} \end{bmatrix}, \tag{6}$$

where S_{ij} is the state of the surface water body at the beginning and end of the study, and n is the number of surface water body types.

2.2.4 Accuracy assessment

The confusion matrix is widely used in the accurate evaluation of remote sensing classification data, and it is an important method for the accurate evaluation of the surface water body data [57]. The confusion matrix with the producer accuracy (PA, equation (7)), the user accuracy (UA, equation (8)), the overall accuracy (OA, equation (9)), and the Kappa coefficient (Kappa, equation (10)) are as follows:

$$\mathrm{PA} = \frac{S_{ij}}{S_i} \times 100\% \tag{7}$$

$$\mathrm{UA} = \frac{S_{ij}}{S_j} \times 100\% \tag{8}$$

$$\mathrm{OA} = \frac{S_{\mathrm{total}}}{n} \tag{9}$$

$$\mathrm{Kappa} = n \times S_{\mathrm{total}} - \sum_{i=1}^{r} \frac{S_i S_j}{n^2} - \sum_{i=1}^{r} S_i S_j \tag{10}$$

where S_{total} is the sum of correctly classified pixels, n is the sum of validation pixels, r is the number of rows, S_{ij} is the observation in row i, column j; S_i is a marginal total of row i; and S_j is a marginal total of column j.

3 Results

3.1 Accuracy of water body mapping in the Xiaolangdi Reservoir

In this study, Sentinel-2 MSI images with a spatial resolution of 10 m were used to verify the water body extraction results of Landsat 30 m spatial resolution. We have considered the 2 km buffer zone of the Landsat Xiaolangdi Reservoir in 2019 as the verification area to ensure the uniform distribution of verification points in water and non-water bodies. We used 2010 Global 30 m land cover remote sensing data product (GlobeLand30) (http://www.globallandcover.com) for the classification of data. The surface cover was divided into the water body and non-water body, and 5,000 verification points were randomly generated, including 1,072 water and 3,928 non-water verification points (Figure 3). Table 1 shows the water body extraction accuracy of the Xiaolangdi Reservoir. The overall accuracy was 98.86%, the producer's accuracy was 95.20%, and the Kappa coefficient was 0.96. It shows that the water body extraction accuracy was relatively high and can be further analyzed.

3.2 Spatiotemporal distribution of the maximum water body in the Xiaolangdi Reservoir

3.2.1 Inter-annual variation of the maximum water body area

The maximum water body area of the Xiaolangdi Reservoir changes greatly from 1999 to 2019. Figure 4 shows that the

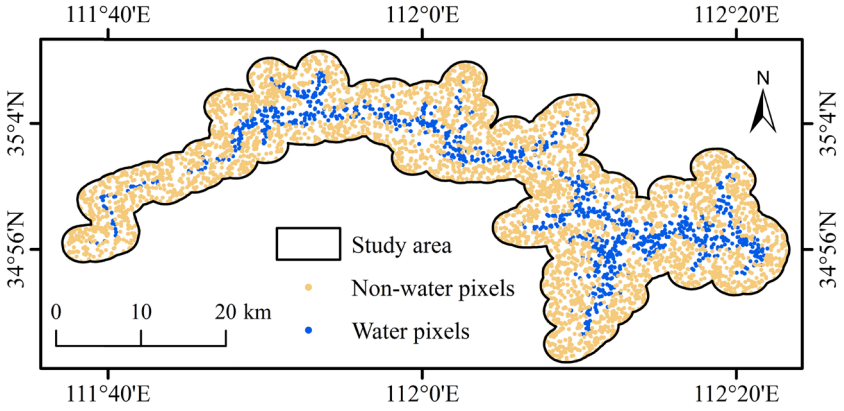

Figure 3: Verification points of the water body and non-water body.

Table 1: The confusion matrix was employed for an accurate evaluation of this study

Landsat	Sentinel-2 MSI		Total	UA
	Water	No-Water		
Water	972	8	980	99.18%
No-Water	49	3971	4,020	98.78%
Total	1,021	3,979	5,000	OA = 98.86%
PA	95.20%	99.80%		Kappa = 0.96

minimum value of the maximum water body area of the Xiaolangdi Reservoir from 1999 to 2019 was 29.14 km^2 (1999), and the maximum was 241.41 km^2 (2017), with an area ratio of 1:8.28 and a difference of 212.27 km^2. From 1999 to 2005, the area of the maximum water body showed an upward trend of 30 km^2/year. From 2005 to 2019, the area of the maximum water body showed a relatively flat change, showing an upward trend of 2.57 km^2/year. Since the construction of the Xiaolangdi Reservoir was completed at the end of 2001, the area of the maximum water body around 2002 was quite different. The average water body area was divided into two phases: 1999–2019 and 2002–2019. This study was consistent with the changing trend of the Xiaolangdi water body researched by Yang et al. [58].

3.2.2 Monthly variation of the maximum water body area

Figure 5a and b shows the monthly distribution of the average maximum water body from February to July and August to January from 2002 to 2019. The maximum water body area of the Xiaolangdi Reservoir has a minimum value of August (106.72 km^2) and a maximum value of March (230.52 km^2). The area ratio was 1:2.16, with a difference of 123.8 km^2. It shows that the area of the largest water body fluctuates greatly during the year.

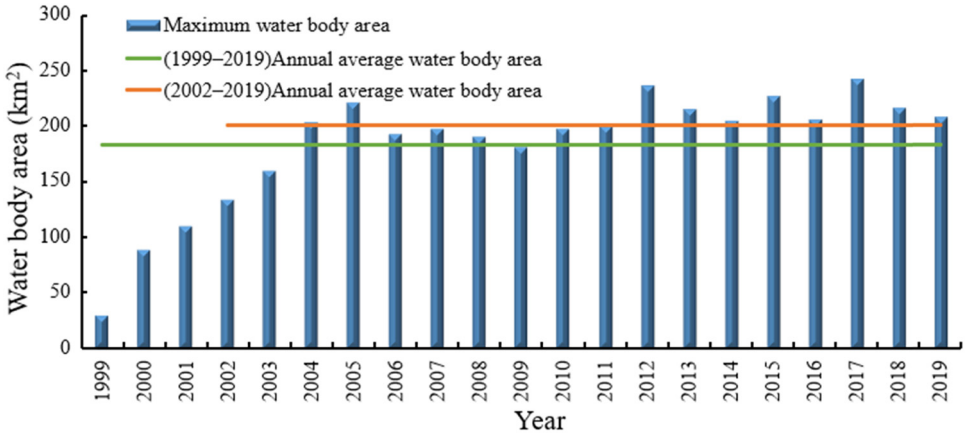

Figure 4: Inter-annual variation of the maximum water body area.

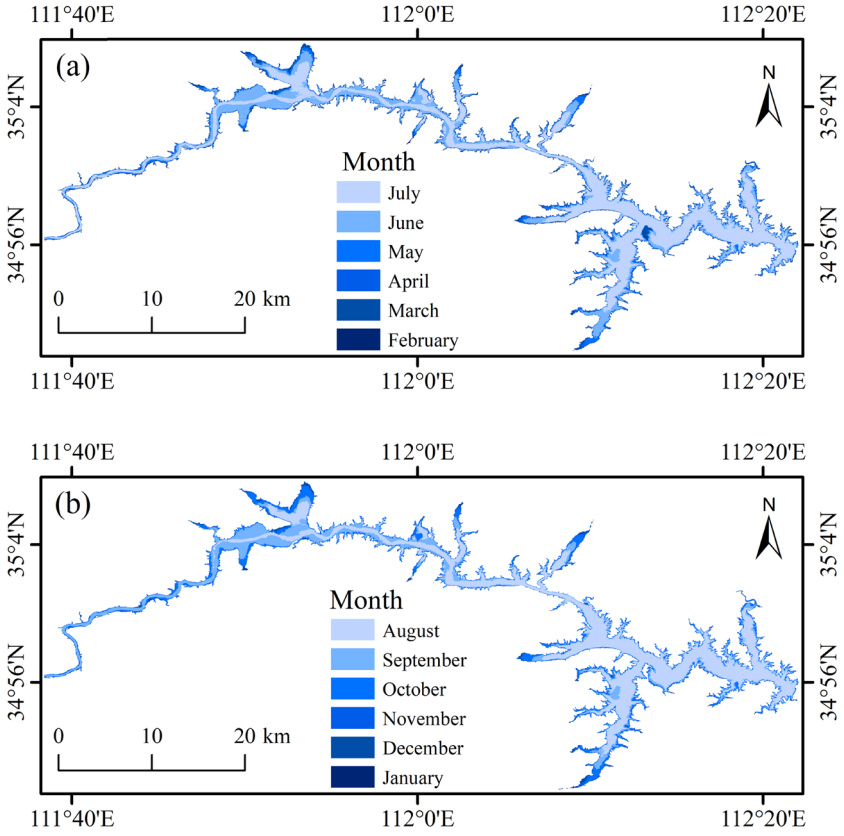

Figure 5: The monthly distribution of the average maximum water body from 2002 to 2019: (a) February to July and (b) August to January.

3.3 Spatiotemporal distribution of the seasonal and permanent water bodies in Xiaolangdi Reservoir

Before and after the completion of the Xiaolangdi Reservoir, the seasonal and permanent water bodies have undergone major changes. Before the completion of the Xiaolangdi Reservoir in 1999, the seasonal water body area and permanent water body area were the smallest, 10.51 and 18.64 km^2, respectively (Figure 6a). After the completion of the Xiaolangdi Reservoir in 2019, the seasonal water body area and permanent water body area were 61.39 and 145.76 km^2, respectively (Figure 6b). Table 2 shows the comparison of the water body area changes in the Xiaolangdi Reservoir in the four periods of 1999–2004, 2005–2009, 2010–2014, and 2015–2019 in this study. The maximum of seasonal and permanent water body area was 2015–2019, and the minimum of seasonal and permanent water body area was 1999–2004. The area of seasonal and permanent water bodies from 1999 to 2019 showed an upward trend, with an increase of 41.32 and 85.35%, respectively. The area of the permanent water body has increased significantly, and the total water body area of the Xiaolangdi Reservoir shows an upward trend, with an increase of 74.29%.

3.4 Conversions of water bodies in the Xiaolangdi Reservoir

Seasonal and permanent water bodies are wetland ecologically staggered zones, and changes in water bodies are indispensable for the movement, living range, and migration of species, and for sustainable development. Figure 7a and b shows the conversion among non-water body, seasonal water body, and permanent water body in the Xiaolangdi Reservoir. During the period of 1999–2004 and 2005–2009, the increased seasonal water body was mainly transformed from the permanent water body, with a conversion area of 7.29 km^2, of which 10.42 km^2 of the seasonal water body was converted into a non-water body. In the period 2005–2009 and 2010–2014, the increased seasonal water bodies were mainly the conversion of permanent water bodies. The conversion area was 6.70 km^2, and only 3.29 km^2 of non-water bodies

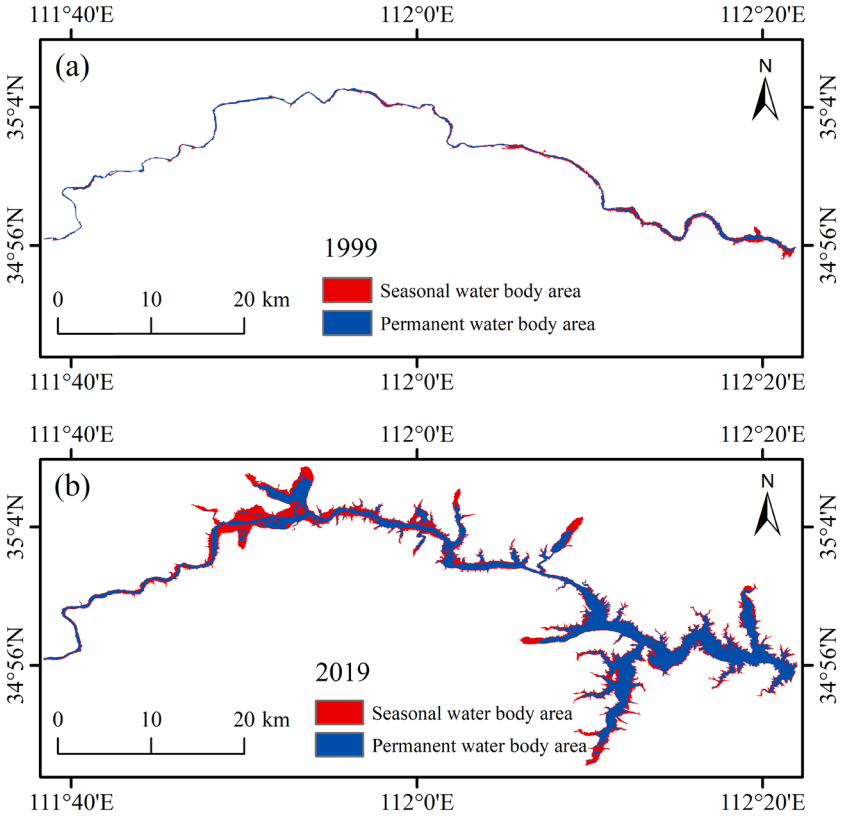

Figure 6: Spatial distribution of seasonal and permanent water body: (a) 1999 and (b) 2019.

were converted into seasonal water bodies. The increased permanent water body was mainly transformed from non-water body and seasonal water body, with conversion areas of 2.69 and 2.27 km^2, respectively. During the period of 2010–2014 and 2015–2019, the increased seasonal water bodies were mainly due to the transformation of permanent water bodies, with a conversion area of 1.98 km^2, and only 0.96 km^2 of non-water bodies converted into seasonal water bodies (Figure 7c). The seasonal water body area increase from 1999 to 2019 was 15.97 km^2, which was mainly formed by the permanent water body transformation. The reduced area of seasonal water bodies was 14.80 km^2, of which 67.56% of seasonal water bodies were converted into non-water bodies; the reduced permanent water body area was 19.53 km^2, of which 75.39% was caused by non-water bodies.

4 Discussion

Many factors affect the water body area changes in the reservoir, which are mainly the changes in precipitation and recharge water in the area and the influence of water consumption for production and domestic use. To determine the changes in the water body area and related factors of the Xiaolangdi Reservoir, we selected 11 indicators that may affect the water body area change (Table 3).

Table 2: Water body area of the Xiaolangdi Reservoir in four periods

Type	Area (km^2)				Percentage change
	1999–2004	2005–2009	2010–2014	2015–2019	1999–2019 (%)
Seasonal	26.21	29.02	32.41	38.54	41.32
Permanent	94.09	166.90	177.55	180.36	85.35
Total	120.30	195.92	209.97	218.91	74.29

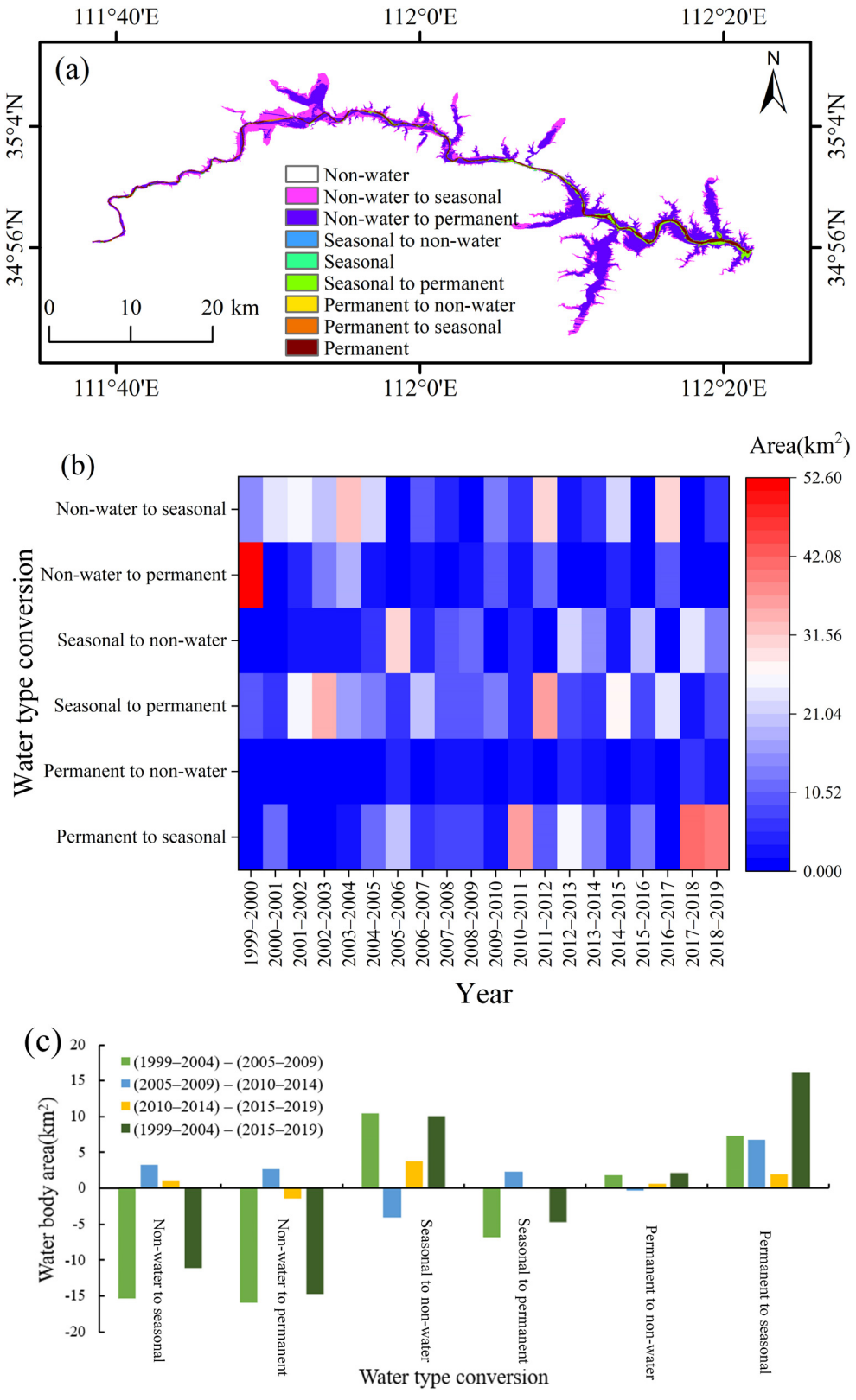

Figure 7: Water body conversion types of the Xiaolangdi Reservoir in the period 1999–2019: (a) spatial patterns of water body transformation; (b) water body transformation matrix; and (c) water body transformation in different periods.

Table 3: Changes in the water body area and related factor statistics of the Xiaolangdi Reservoir

	Water body area of the Xiaolangdi Reservoir		
	Pearson correlation	**Significant**	***N***
Runoff	0.731	0.266	15
Precipitation	−0.007	0.975	21
Temperature	−0.061	0.794	21
Population	−0.670***	0.001	21
GDP	0.677***	0.001	21
Gross value of the primary industry	0.684***	0.001	21
Gross value of the secondary industry	0.700***	0.000	21
Gross value of the tertiary industry	0.532**	0.013	21
Per capita GDP	0.661***	0.001	21
Grain sown area	0.237	0.301	21

Note: "**" and "***" Significance levels at 0.05, and 0.01, respectively. $N = 15$ (2005–2019); $N = 21$ (1999–2019).

It includes three items of nature and seven items of human factors. Pearson correlation analysis is carried out by using SPSS software. The spatial scope includes the Henan Province (Mengjin County, Xin'an County, Mianchi County, and Jiyuan City) and the Shanxi Province (Xia County and Yuanqu County) around the reservoir. The natural factor data are derived from the GLDAS data in the GEE platform and the annual runoff data are from the Yellow River Conservancy Commission of the Ministry of Water Resources. The data of anthropogenic factors mainly refer to the statistical yearbooks of Henan and Shanxi provinces from 1999 to 2019 to analyze the correlation between the reservoir body area and the main economic and social indicators.

As shown in Table 3, (1) the water body area of the Xiaolangdi Reservoir is weakly, negatively correlated with precipitation and temperature, which shows that the influence of natural factors on the change of the water body area is not obvious. (2) The annual variation of runoff of the Xiaolangdi water station shows that the average runoff from 1987 to 2015 is $244.4 \times 10^8\,m^3$, the runoff from 2005 is $221.3 \times 10^8\,m^3$, and the runoff from 2019 is $459.2 \times 10^8\,m^3$. The runoff into the reservoir increased gradually from 2005 to 2019. The direct reason for the increasing area of the Xiaolangdi Reservoir in recent 20 years is the gradual increase of the runoff into the reservoir. (3) There was a weak positive correlation between the sown area of grain and the water body area. The correlation analysis showed that the increase of the sown area of grains and the water body area were associated, which indicated that the important reason for the change of the water area was the change of the cultivated area. (4) With the rapid development of society and economy, the demand for water resources in the Xiaolangdi area is increasing. Irrigation accounts for most of the total water withdrawals because wheat and corn are the main crops, and irrigation requires a lot of groundwater. The total population of the Xiaolangdi area in 2019 is nearly 74,000 less than that in 1999. There is a positive correlation between total population and water consumption. The decrease of population means the decrease of water consumption, which is the indirect driving force of the increase of water body area; (5) the water body area of the Xiaolangdi Reservoir is strongly and positively correlated with the gross domestic product (GDP), the gross value of the primary industry, the gross value of the secondary industry, the gross value of the tertiary industry, and per capita GDP of the Xiaolangdi area. The GDP of the Xiaolangdi Reservoir area was 30.83×10^8 yuan in 1999, 113.17×10^8 yuan in 2010, and 157.72×10^8 yuan in 2019, which is about five times that of 1999. After the completion of the Xiaolangdi Reservoir, the secondary industry developed rapidly, accounting for 58.81% in 1999, 68.18% in 2010, and 80.13% in 2019. The development of the Xiaolangdi tourism industry has driven the development of the surrounding economy, increased the surrounding fiscal revenue, promoted local employment, and improved the living standard of surrounding residents.

5 Conclusion

This study investigated the inter-annual and intra-annual spatial changes in the water body area in the Xiaolangdi Reservoir from 1999 to 2019 based on all available Landsat TM, ETM+, and OLI images in the GEE platform. The overall accuracy of Xiaolangdi Reservoir's water body extraction was 98.86%, the producer's accuracy was 95.20%, and the Kappa coefficient was 0.96, indicating that the water body extraction results are more accurate and suitable for water body extraction in the Xiaolangdi Reservoir. The water bodies were classified into the maximum water body, seasonal water body, and permanent water body according to the inundation frequency. The maximum water body area of the Xiaolangdi Reservoir varies greatly between inter-annual and intra-annual, and seasonal and permanent water bodies have uneven spatiotemporal distribution. In the conversion of water

body types, the seasonal water body area increased by the Xiaolangdi Reservoir from 1999 to 2019 was 15.97 km^2, which was mainly formed by permanent water body conversion, and the reduced permanent water body area was 19.53 km^2, of which 75.39% was caused by non-water conversion. The change of the water body area of the Xiaolangdi Reservoir has a weak negative correlation with natural factors such as precipitation and temperature, and population, and it was positively correlated with seven indicators such as runoff and regional GDP.

The results of this study provide a scientific basis for the ecological protection, water resources management, and decision-making planning of the Xiaolangdi Reservoir in the Yellow River Basin. However, there are some shortcomings. The mixed pixels at the edge of the water body are the main reason for the classification error of the pixels. The next step can be combined with deep learning, neural network, and other algorithms for water body research.

Acknowledgments: We thank the editors and the anonymous reviewers for their valuable comments and suggestions.

Funding information: This research was funded by "Henan Provincial Department of Science and Technology Research Project (212102310019)," "Natural Science Foundation of Henan (202300410531)," "Youth Science Foundation Program of Henan Natural Science Foundation (202300410077)," "the major project of Collaborative Innovation Center on Yellow River Civilization jointly built by Henan Province and Ministry of Education (2020M19)," "College Students' Innovative Entrepreneurial Training Plan Program (202010475141)," "Dabieshan National Observation and Research Field Station of Forest Ecosystem at Henan," and "Data Center of Middle & Lower Yellow River Regions, National Earth System Science Data Center, National Science & Technology Infrastructure of China (http://henu.geodata.cn, accessed on 14 October 2020)."

Author contributions: This research was carried out under the cooperation of all authors. H.X., and T.C. provided the writing ideas for the research; R.W., and H.X. completed data collection, analysis and wrote the paper; and L.P., W.N., R.L., X.Z., X.B., C.Y., T.C., Y.S., and H.X. contributed to the discussion and revision of the paper. All authors have read and agreed to the published version of the manuscript.

Conflict of interest: Authors state no conflict of interest.

References

[1] Zhang YF, Qi QQ, Zhang ZZ. The research of Xiaolangdi Reservoir environmental compensation benefits. Adv Mat Res. 2012;599:678–81.

[2] Chen JG, Zhou WH, Qiang C. Sedimentation and transformation of morphology in the lower Yellow River during 10 year's initial operation of the Xiaolangdi Reservoir. J Hydrodynam. 2012;24(6):914–24.

[3] Liu Y, Fan H, Wang L, Zhuang H. Monitoring of surface deformation in a low coherence area using distributed scatterers InSAR: case study in the Xiaolangdi basin of the Yellow River, China. Bulletin Eng Geol Environ. 2020;80(1):25–39.

[4] Liang C, Xin S, Dongsheng W, Xiuying Y, Guodong J. The ecological benefit–loss evaluation in a riverine wetland for hydropower projects – a case study of Xiaolangdi Reservoir in the Yellow River, China. Ecol Eng. 2016;96:34–44.

[5] Zhou Y, Huang HQ, Ran L, Shi C, Su T. Hydrological controls on the evolution of the Yellow River delta: an evaluation of the relationship since the Xiaolangdi Reservoir became fully operational. Hydrol Process. 2018;32(24):3633–49.

[6] Kong D, Miao C, Wu J, Borthwick AGL, Duan Q, Zhang X. Environmental impact assessments of the Xiaolangdi Reservoir on the most hyperconcentrated Laden River, Yellow River, China. Environ Sci Pollut Res. 2017;24(5):4337–51.

[7] Wang Y, Wu B, Zhong D. Adjustment in the main-channel geometry of the lower Yellow River before and after the operation of the Xiaolangdi Reservoir from 1986 to 2015. J Geogr Sci. 2020;30(3):468–87.

[8] Ludwig HF, Gunaratnam D, Yuming S. Environmental impact assessment for Xiaolangdi Yellow River multi-purpose economic-cum environmental improvement project. Environmentalist. 1995;15(1):45–57.

[9] Xia H, Zhao W, Li A, Bian J, Zhang Z. Subpixel inundation mapping using landsat-8 OLI and UAV data for a wetland region on the Zoige plateau, China. Remote Sens. 2017;9(1):31.

[10] Xia H, Qin Y, Feng G, Meng Q, Cui Y, Song H, et al. Forest phenology dynamics to climate change and topography in a geographic and climate transition zone: the Qinling mountains in central China. Forests. 2019;10(11):1007.

[11] Harvey KR, Hill GJE. Vegetation mapping of a tropical freshwater swamp in the Northern Territory, Australia: a comparison of aerial photography, Landsat TM and SPOT satellite imagery. Int J Remote Sens. 2001;22(15):2911–25.

[12] Mueller N, Lewis A, Roberts D, Ring S, Melrose R, Sixsmith J, et al. Water observations from space: mapping surface water from 25 years of Landsat imagery across Australia. Remote Sens Environ. 2016;174:341–52.

[13] Hall JW, Grey D, Garrick D, Fung F, Brown C, Dadson SJ, et al. Coping with the curse of freshwater variability. Science. 2014;346(6208):429–30.

[14] Zou Z, Dong J, Menarguez MA, Xiao X, Qin Y, Doughty RB, et al. Continued decrease of open surface water body area in Oklahoma during 1984-2015. Sci Total Environ. 2017;595:451–60.

[15] Deng Y, Jiang W, Tang Z, Ling Z, Wu Z. Long-term changes of open-surface water bodies in the Yangtze River basin based on the Google Earth Engine cloud platform. Remote Sens. 2019;11(19):2213.

[16] Wang X, Xiao X, Zou Z, Dong J, Qin Y, Doughty RB, et al. Gainers and losers of surface and terrestrial water resources in China during 1989–2016. Nat Commun. 2020;11(1):1–12.
[17] Wang R, Xia H, Qin Y, Niu W, Pan L, Li R, et al. Dynamic monitoring of surface water area during 1989–2019 in the hetao plain using landsat data in Google Earth Engine. Water. 2020;12(11):3010.
[18] Chen B, Chen L, Huang B, Michishita R, Xu B. Dynamic monitoring of the Poyang lake wetland by integrating Landsat and MODIS observations. ISPRS J Photogramm Remote Sens. 2018;139:75–87.
[19] Li S, Sun D, Goldberg M, Stefanidis A. Derivation of 30-m-resolution water maps from TERRA/MODIS and SRTM. Remote Sens Environ. 2013;134:417–30.
[20] Klein I, Mayr S, Gessner U, Hirner A, Kuenzer C. Water and hydropower reservoirs: high temporal resolution time series derived from MODIS data to characterize seasonality and variability. Remote Sens Environ. 2021;253:112207.
[21] Bansal S, Katyal D, Garg JK. A novel strategy for wetland area extraction using multispectral MODIS data. Remote Sens Environ. 2017;200:183–205.
[22] Yang X, Qin Q, Yésou H, Ledauphin T, Koehl M, Grussenmeyer P, et al. Monthly estimation of the surface water extent in France at a 10-m resolution using Sentinel-2 data. Remote Sens Environ. 2020;244:111803.
[23] Du Y, Zhang Y, Ling F, Wang Q, Li W, Li X. Water bodies' mapping from Sentinel-2 imagery with modified normalized difference water index at 10-m spatial resolution produced by sharpening the SWIR band. Remote Sens. 2016;8(4):354.
[24] Sekertekin A. Potential of global thresholding methods for the identification of surface water resources using Sentinel-2 satellite imagery and normalized difference water index. J Appl Remote Sens. 2019;13(4):044507.
[25] Yang X, Chen L. Evaluation of automated urban surface water extraction from Sentinel-2A imagery using different water indices. J Appl Remote Sens. 2017;11(2):026016.
[26] Jagadeesha CJ, Palnitkar VG. Satellite data aids in monitoring reservoir water and irrigated agriculture. Water Int. 1991;16(1):27–37.
[27] Wang X, de Linage C, Famiglietti J, Zender CS. Gravity recovery and climate experiment (GRACE) detection of water storage changes in the Three Gorges Reservoir of china and comparison with in situ measurements. Water Resour Res. 2011;47(12):WI2502.
[28] Longuevergne L, Wilson CR, Scanlon BR, Crétaux JF. GRACE water storage estimates for the middle east and other regions with significant reservoir and lake storage. Hydrol Earth Syst Sci. 2013;17(12):4817–30.
[29] Zhang H, Gorelick SM, Zimba PV, Zhang X. A remote sensing method for estimating regional reservoir area and evaporative loss. J Hydrol. 2017;555:213–27.
[30] Bhadoriya UPS. Implications of climate change on water storage and filling time of a multipurpose reservoir in India. J Hydrol. 2020;590:125542.
[31] Hou X, Feng L, Duan H, Chen X, Sun D, Shi K. Fifteen-year monitoring of the turbidity dynamics in large lakes and reservoirs in the middle and lower basin of the Yangtze River, China. Remote Sens Environ. 2017;190:107–21.
[32] Dong J, Xia X, Zhang Z, Liu Z, Zhang X, Li H. Variations in concentrations and bioavailability of heavy metals in rivers caused by water conservancy projects: Insights from water regulation of the Xiaolangdi Reservoir in the Yellow River. J Environ Sci. 2018;74:79–87.
[33] Gorelick N, Hancher M, Dixon M, Ilyushchenko S, Thau D, Moore R. Google Earth Engine: planetary-scale geospatial analysis for everyone. Remote Sens Environ. 2017;202:18–27.
[34] Pekel J-F, Cottam A, Gorelick N, Belward AS. High-resolution mapping of global surface water and its long-term changes. Nature. 2016;540(7633):418–22.
[35] Mutanga O, Kumar L. Google Earth Engine applications. Remote Sens. 2019;11:591.
[36] Xia H, Zhao J, Qin Y, Yang J, Cui Y, Song H, et al. Changes in water surface area during 1989–2017 in the Huai River basin using landsat data and Google Earth Engine. Remote Sens. 2019;11(15):1824.
[37] Xiong J, Thenkabail PS, Gumma MK, Teluguntla P, Poehnelt J, Congalton RG, et al. Automated cropland mapping of continental Africa using Google Earth Engine cloud computing. ISPRS Int J Geoinf. 2017;126:225–44.
[38] Shelestov A, Lavreniuk M, Kussul N, Novikov A, Skakun S. Exploring Google Earth Engine platform for big data processing: classification of multi-temporal satellite imagery for crop mapping. Front Earth Sci. 2017;5:17.
[39] Pan L, Xia H, Zhao X, Guo Y, Qin Y. Mapping winter crops using a phenology algorithm, time-series Sentinel-2 and Landsat-7/8 Images, and Google Earth Engine. Remote Sens. 2021;13(13):2510.
[40] Pan L, Xia H, Yang J, Niu W, Wang R, Song H, et al. Mapping cropping intensity in Huaihe basin using phenology algorithm, all Sentinel-2 and Landsat images in Google Earth Engine. Int J Appl Earth Obs Geoinf. 2021;102:102376.
[41] Zhao X, Xia H, Pan L, Song H, Niu W, Wang R, et al. Drought monitoring over Yellow River basin from 2003–2019 using reconstructed MODIS land surface temperature in Google Earth Engine. Remote Sens. 2021;13(18):3748.
[42] Niu W, Xia H, Wang R, Pan L, Meng Q, Qin Y, et al. Research on large-scale urban shrinkage and expansion in the Yellow River affected area using night light data. ISPRS Int J Geo-Inf. 2021;10(1):5.
[43] Hird J, DeLancey E, McDermid G, Kariyeva J. Google Earth Engine, open-access satellite data, and machine learning in support of large-area probabilistic wetland mapping. Remote Sens. 2017;9(12):1315.
[44] Guo Y, Xia H, Pan L, Zhao X, Li R, Bian X, et al. Development of a new phenology algorithm for fine mapping of cropping intensity in complex planting areas using Sentinel-2 and Google Earth Engine. ISPRS Int J Geo-Inf. 2021;10(9):587.
[45] Gómez C, White JC, Wulder MA. Optical remotely sensed time series data for land cover classification: a review. ISPRS J Photogramm Remote Sens. 2016;116:55–72.
[46] Hinton GE, Salakhutdinov RR. Reducing the dimensionality of data with neural networks. Science. 2006;313(5786):504–7.
[47] Khatami R, Mountrakis G, Stehman SV. A meta-analysis of remote sensing research on supervised pixel-based land-cover image classification processes: general guidelines for practitioners and future research. Remote Sens Environ. 2016;177:89–100.

[48] McFeeters SK. The use of the normalized difference water index (NDWI) in the delineation of open water features. Int J Remote Sens. 2007;17(7):1425–32.
[49] Xu H. Modification of normalised difference water index (NDWI) to enhance open water features in remotely sensed imagery. Int J Remote Sens. 2007;27(14):3025–33.
[50] Han Q, Niu Z. Construction of the long-term global surface water extent dataset based on water-NDVI spatio-temporal parameter set. Remote Sens. 2020;12(17):2675.
[51] Dwyer JL, Roy DP, Sauer B, Jenkerson CB, Zhang HK, Lymburner L. Analysis ready data: enabling analysis of the Landsat archive. Remote Sens. 2018;10(9):1363.
[52] Wulder MA, White JC, Loveland TR, Woodcock CE, Belward AS, Cohen WB, et al. The global landsat archive: status, consolidation, and direction. Remote Sens Environ. 2016;185:271–83.
[53] Rodell M, Houser PR, Jambor U, Gottschalck J, Mitchell K, Meng CJ, et al. The global land data assimilation system. Bull Am Meteorol Soc. 2004;85(3):381–94.
[54] Jun C, Ban Y, Li S. Open access to earth land-cover map. Nature. 2014;514:434–4.
[55] Liao A, Chen L, Chen J, He C, Cao X, Chen J, et al. High-resolution remote sensing mapping of global land water. Sci China Earth Sci. 2014;57(10):2305–16.
[56] Zhou Y, Dong J, Xiao X, Liu R, Zou Z, Zhao G, et al. Continuous monitoring of lake dynamics on the Mongolian Plateau using all available Landsat imagery and Google Earth Engine. Sci Total Environ. 2019;689:366–80.
[57] Su K, Wei DZ, Lin WX. Evaluation of ecosystem services value and its implications for policy making in China – a case study of Fujian province. Ecol Indic. 2020;108:105752.
[58] Yang Y, Wang Z, Yang H, Wang F, Li R. Water body and vegetation dynamic changes in lake and reservoir of the Yellow River under climate change. Yellow River. 2019;8:10.